Pergamon

*Journal of Structural Geology*, Vol. 16, No. 3, pp. 287 to 301, 1994

0191-8141/94 $06.00 + 0.00

# Flow laws for rocks containing two non-linear viscous phases: a phenomenological approach

MARK R. HANDY*

Geologisches Institut, Universität Bern, Bern, Switzerland

(*Received* 2 *December* 1991; *accepted in revised form* 5 *May* 1993)

**Abstract**—Mylonitic rocks and rock-analogue materials reveal two basic types of structure: (1) a load-bearing framework (LBF) of strong phase contains isolated pockets of weak phase; (2) interconnected layers of weak phase (IWL) separate boudins and clasts of strong phase. Aggregates with the LBF microstructure are characterized by nearly uniform strain rate. Stress is concentrated in the load-bearing framework. In aggregates with an IWL microstructure, strain rate and sometimes also stress are higher in the interconnected weak phase than in the boudins and clasts of strong phase. The degree of stress and strain partitioning depends strongly on the viscous strength contrast and on the relative amounts of the constituent mineral phases. Based on these observations, the rheology of two-phase rock is modelled with separate functions for LBF and IWL microstructures. A new flow law is derived for rock with IWL structure in which two phases undergo dislocation creep. The flow law expresses composite creep strength in terms of temperature, bulk strain rate and the volume proportions and creep parameters of the minerals in the rock. Strain rate and stress are averaged in the constituent phases and slip along phase boundaries maintains strain compatibility within the aggregate. Composite strengths predicted with the IWL flow law fall well within the uniform stress and uniform strain rate bounds and are generally consistent with the viscous strengths of experimentally deformed bimineralic aggregates. A hypothesis of viscous strain energy minimization is used to determine the relative stability of the LBF and IWL microstructures. During steady-state creep, the IWL microstructure is predicted to be stable over a broad range of two-phase compositions and mineral strength contrasts, whereas the LBF microstructure is stable only in rocks with low volume proportions of weak phase and low to moderate mineral strength contrasts. The IWL flow law indicates that rheological stratification in the lithosphere depends strongly on rock composition, especially in rocks with low volume proportions of a weak phase and high mineral strength contrasts.

## INTRODUCTION

MOST rocks in the intermediate to deep crust and in the mantle contain one or more mineral or melt phases with non-linear temperature, strain rate and grain size dependent rheologies. The problem of deriving a flow law for such viscous composite materials has vexed physicists, engineers and earth scientists for many years and approaches to an analytical solution have advanced along both experimental and theoretical lines (review in Handy 1990).

The investigation of composite materials reveals that their rheology is intimately related to their structure. Two basic kinds of microstructure are distinguished in naturally and experimentally deformed two-phase aggregates (Fig. 1, simplified from Handy 1990): (1) the stronger phase forms a load-bearing framework (LBF structure) that contains pockets of the weaker phase; (2) the weaker phase forms an interconnected weak matrix or layers (IWL structure) separating boudins or clasts of the stronger phase. In this paper, a 'phase' is any material with distinctive rheological properties. The adjectives 'weak' and 'strong' describe the relative strengths of two phases outside their host composite material at a reference strain rate and temperature. The ratio of these strengths is the viscous strength contrast, $\tau_c$, or competence contrast of the two materials (see Ramsay & Huber 1987, p. 7) and is an absolute measure of their relative deformability.

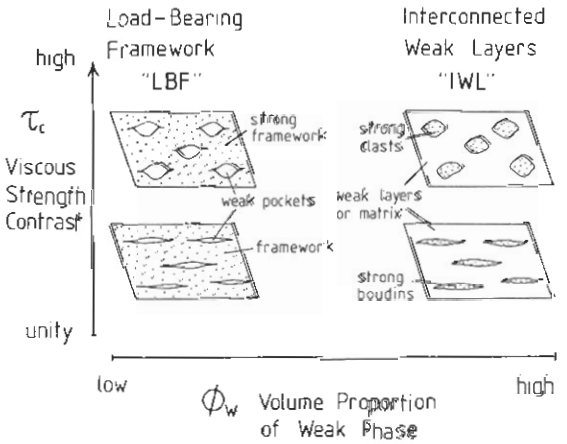


Fig. 1. Microstructures in deformed two-phase viscous materials as a function of the volume proportion of the weaker phase ($\phi_w$, horizontal axis) and viscous strength contrast between the strong and weak phases ($\tau_c$, vertical axis). LBF and IWL are abbreviations for 'load-bearing framework' and 'interconnected weak layer' microstructures.

For a given bulk strain, the aspect ratio of the isolated phases within both LBF and IWL structures is inversely and non-linearly related to the viscous strength contrast between the constituent phases at the bulk strain rate (Gay 1968, Bilby *et al.* 1975, Freeman 1987) (Fig. 1). Stress and strain partitioning amongst the phases depends on the contrast in rheological properties of the constituent phases (Cobbold 1983, Treagus & Sokoutis 1992, Weijermars 1992) and on the volume proportions of the phases in the composite material. At strength

*Current address: Institut für Geowissenschaften, Justus-Liebig-Universität, Senckenbergstrasse 3, D-35390 Giessen, Germany.

ratios near unity, both phases deform almost homogeneously and form lenticular, interconnected layers that are oriented subparallel to the plane of shear, regardless of their relative abundance in the rock (fig. 1.8 in Ramsay & Huber 1987).

In view of this close relationship between structure and rheology, it seems surprising that rock composition and structure are not incorporated into current rheological models of Earth's lithosphere. This reflects the mathematical complexity of modelling heterogeneous flow in composite materials like rock, whose constituent phases usually have non-linear, viscoplastic rheologies (review in Carter & Tsenn 1987). A common, relatively simple approach to determining the bulk rheology of such material involves the limiting assumptions that either strain rate or stress is homogeneous within the aggregate. These end-member conditions, corresponding respectively to the Voigt and Reuss elastic bounds (e.g. Hill 1965), provide rigorous upper and lower limits to the actual viscous strength of the rock. At both bounds, the strength of the composite depends on the volume proportions and rheologies of the constituent phases (e.g. see equations 2–6 in Tullis *et al.* 1991). In the upper bound case, each grain or phase in the aggregate deforms compatibly with its neighbour, whereas at the lower bound, every phase is subject to the same stress, regardless of its rheology, shape or position in the microstructure. Of course, neither bounding condition is realistic. The dissimilar rheologies of the constituent phases give rise to stress differences and strain incompatibilities within the aggregate. In naturally deformed rock, such incompatibilities are relaxed by slip at phase boundaries, dynamic recovery and recrystallization, texture weakening, pressure solution and cataclasis (e.g. White *et al.* 1980). Thus, the bulk strength of non-linear viscous materials lies somewhere between the viscous strength at the uniform strain rate and uniform stress bounds. Although these bounds certainly provide closer constraints on actual bulk strength than extrapolated flow laws for the constituent phases, the bounding theorems method becomes less accurate as the bounds diverge with increasing contrast in the rheological properties of the phases. Averaging the bulk strength at the two bounds (Voigt–Reuss–Hill method) yields reasonable estimates of composite strength, but is physically unfounded and implies that the strength of the constituent phases lies between their individual strengths at the bounds. As demonstrated in the next section, this is untenable for rock with an IWL microstructure.

Another approach is the self-consistent theory, so called because the average stress and strain rate of the matrix surrounding any given grain within a polyphase aggregate are equated with the stress and strain rate of the aggregate itself. This constrains the behaviour of any given grain to satisfy both stress equilibrium and strain compatibility with the aggregate as a whole, rather than with its neighbouring grains. Because strain compatibility is only maintained on the aggregate scale, local compatibility is relaxed, allowing weak grains to deform faster than strong grains. The bulk stress is calculated after each strain increment along a predetermined strain path and adjusted to satisfy bulk compatibility. Self-consistent theory was originally conceived to describe the elastoplastic deformation of composite material (Kröner 1961). It has successfully predicted the strength of metallic and ceramic polycrystals between the uniform strain rate and stress bounds (e.g. Hutchinson 1976). Recently, the self-consistent theory has been extended to large strain, viscoplastic deformation of composite materials (Molinari *et al.* 1987). Viscoplastic self-consistent (VPSC) theory has proved useful in simulating texture in polycrystalline, monomineralic rock (quartzite, Wenk *et al.* 1989) and polymineralic rock (peridotite, Wenk *et al.* 1991). However, the basic problem with using current VPSC theory to predict viscous composite strengths is that it neglects the effects of domainal structural heterogeneity on stress and strain partitioning within the aggregate. Self-consistency constrains weak grains always to deform at lower stresses than stronger grains. This contrasts with microstructural observations below which suggest that on the supragranular scale, an interconnected matrix of weak grains can support higher flow stress than boudinaged layers of strong grains. The conceptual implications this bears for realistic modelling of heterogeneous polyphase flow are explored in the latter part of this paper.

Tullis *et al.* (1991) performed finite element modelling of both real and hypothetical two-phase microstructures to arrive at a simple empirical solution: the flow law for a two-phase rock is approximated by a power law that passes through the equiviscous point of the constituent phases on a stress vs strain rate diagram and has a creep exponent that is the volume-weighted, geometric mean of the end-member creep exponents (their equations 10–12). The authors point out, however, that this flow law does not strictly apply to the IWL microstructure (Fig. 1) at moderate to high mineral strength contrasts. This microstructure is ubiquitous in naturally deformed rocks over a broad range of compositions, homologous temperatures and strain rates (Handy 1990).

A common feature of all the analytical solutions reviewed above is that bulk strength is modelled as a single, continuous function of composition, irrespective of the microstructure. To the extent that microstructure is specified at all (e.g. Wenk *et al.* 1991), no distinction is made between LBF and IWL microstructures. Yet the microstructures in naturally deformed rock indicate that stress and strain partition quite differently in these two microstructures (Handy 1990), especially in rocks with phases having moderate to high mineral strength contrasts ($\tau_c \geq 5$). Therefore, two constitutive equations corresponding to these microstructures may provide a more realistic description of heterogeneous creep in mylonite.

This paper adopts a phenomenological approach in placing quantitative constraints on the rheology of bimineralic mylonite. Microstructural observations in naturally deformed rocks are used to show how stress, strain and strain rate partition in rheologically and

structurally heterogeneous material. These observations provide a conceptual basis for deriving flow laws for two-phase aggregates with idealized LBF and IWL microstructures. The IWL flow law is compared with the available rheological data for experimentally and naturally deformed bimineralic aggregates, as well as with empirical and analytical solutions in the literature for the creep of polyphase rock. The relative stability of LBF and IWL microstructures at steady-state creep is examined in the context of a strain energy minimization criterion for microstructural equilibrium. Finally, the two-phase flow laws are used to estimate the effect of varied rock composition on the rheology of the lithosphere.

## STRESS, STRAIN AND STRAIN RATE PARTITIONING IN MYLONITE

Boudins in mylonite comprise either the same mineral as the matrix (Fig. 2) or a different mineral (Fig. 3). This structural heterogeneity reflects microscale rheological contrasts that are inferred to evolve from the nucleation and growth of rheological instabilities during progressive shearing (Fig. 2) or to stem from mineralogical heterogeneity that existed prior to shearing (Fig. 3). Measurement of the size of subgrains and dynamically recrystallized grains in different microstructural domains allows one to quantify the partitioning of creep stress in the rock during mylonitization provided that: (1) the grain size froze simultaneously in these domains at the end of mylonitization; and (2) subsequent deformation or annealing did not alter stress-sensitive microstructures. Grain size is related to creep stress via the empirically and theoretically derived relation (e.g Twiss 1977, 1986):

$$\tau = 3^{-1/2} L \delta^{-p}, \qquad (1)$$

where $\delta$ is the diameter of subgrains or dynamically recrystallized grains and $\tau$ is the creep stress of the material in simple, octahedral shear. The empirically derived material constants, $L$ and $p$, are only valid for the dynamic recovery and recrystallization mechanism reported in the experimental calibrations in the literature (references in Fig. 4). For quartz analysed in Fig. 2, this mechanism is progressive subgrain rotation and subsequent grain growth (dynamic recrystallization regime 2 of Hirth & Tullis 1992). The subgrains were measured with an optical microscope and had crystallographic misorientations with neighbouring grains of about 1–10°. Thus, the stress estimates reported below from optical subgrains cannot be compared with stress values determined from smaller subgrains visible only with a transmission electron microscope (e.g. White 1976). In all analyses made here, the grain size measured in thin section was corrected for the two-dimensional truncation effect (Exner 1972, pp. 32–33).

The piezometric relation in equation (1) is only applicable to mylonitic rocks like those in Figs. 2 and 3 for which the dominant strain accommodating mechanism was dislocation recovery and creep. The strongly asymmetrical crystallographic and shape preferred orientations of quartz measured in these samples (*c*-axis patterns in fig. 6 of Handy 1990, fig. 8 of Handy & Zingg 1991) is diagnostic of dislocation creep during predominantly non-coaxial shear. Strain partitioning in these rocks can only be estimated qualitatively because: (1) there are no passive strain markers; and (2) the current grain shape may be the product of several cycles of grain coalescence and recrystallization (Urai *et al.* 1986). Despite these limitations, the qualitative conclusions drawn at the end of this section regarding stress and strain rate partitioning are expected to apply to any polyphase material undergoing dislocation creep.

### *Mylonite with low mineral strength contrast*

Mylonite with low mineral strength contrasts commonly occurs in shear zones where high homologous temperatures and small grain sizes reduced strength ratios to less than an order of magnitude (e.g. quartz–feldspar mylonite in fig. 3 of Handy 1990). Unfortunately, estimating creep stress in all minerals of granitic or peridotitic mylonite is still impossible because experimentally calibrated piezometers are currently available for only one of the strain-accommodating minerals (quartz, olivine). A viable alternative is therefore to examine heterogeneously deformed monomineralic mylonite like the quartzite in Fig. 2. The same piezometers can be used to compare stress in all microstructural domains.

The quartz mylonite in Fig. 2 was deformed at mid- to upper-greenschist facies conditions (*ca* 350°C). Figure 2(a) shows that the domains of unrecrystallized quartz comprise ribbon grains with high aspect ratios as well as globular grains with lower aspect ratios. These globular grains locally deflect the ribbons and the interconnected, dynamically recrystallized layers. The size of dynamically recrystallized grains and subgrains in the interconnected matrix is smaller in these deflected regions than in the undisrupted, planar regions between ribbon grains (compare area 2 with areas 1 and 3, Figs. 2a and 4). This indicates that the creep stress is higher in the matrix adjacent to the more competent globular grain than in the vicinity of the less competent ribbons. The subgrains in the globular grain are consistently larger than in the ribbon grains (compare areas 4 and 5, Figs. 2a and 4). Observed in detail, the subgrain size generally decreases towards the edges of the globular and ribbon grains (Fig. 2b). The marginal grain size gradients are steeper in the globular grain than in the ribbons, but the poor definition and irregular shape of the subgrains near the ribbon rims preclude any reliable quantification of these gradients under the optical microscope.

The variation in subgrain size amongst the domains in Fig. 2(a) is believed to reflect local stress gradients within the rock during mylonitization because: (1) there is no evidence for post-tectonic annealing and grain growth in any domain (i.e. neither straight grain bound-

aries nor stable grain boundary triple junctions were observed); (2) the size distribution of optical subgrains is unimodal within each microstructural domain. The first point indicates that the stress drop at the end of deformation was sufficiently fast to prevent the subgrain size in ribbon and globular grains from re-equilibrating with stress much later than in the matrix. The temperature at the end of mylonitization was also sufficiently low, or decreased quickly enough, to inhibit annealing. The second point suggests that post-mylonitic stresses were never high enough to reset the microstructures. Therefore, the aforementioned subgrain size gradients in the rims of the globular and ribbon grains are interpreted to reflect sharp increases in creep stress from the more competent domains to the incompetent, dynamically recrystallized matrix. The disparity in the creep stresses between the contiguous matrix and the elongate, unrecrystallized grains suggests that there may have been considerable slip along their mutual boundaries.

*Mylonite with high mineral strength contrast*

Flow in quartz–feldspar granitic rock sheared at mid- to upper-greenschist facies conditions is much more heterogeneous than in the pure quartz mylonite above (compare Figs. 2a and 3). Quartz forms an interconnected matrix of dynamically recrystallized grains that envelop rounded feldspar grains. This reflects the high strength contrast between quartz and feldspar at these conditions. The quartz grains are both smaller and more elongate between the impinging feldspar grains than where the feldspar grains are further apart (Fig. 3). Thus, stress, strain, and strain rate were locally much higher in the quartz matrix between the feldspar grains than elsewhere. As in Fig. 2 above, the preservation of unstable grain boundaries and triple junctions in quartz indicates that the stress drop at the end of deformation was fast enough to freeze in stress-dependent grain size gradients on a very small scale (Handy 1990, Prior *et al.* 1990). In contrast to quartz, the feldspar grains show few traces of internal strain. Although the feldspar grains sometimes contain evidence for local stress concentration (e.g. stress twinning near mica inclusions), the average stress within these grains during mylonitization is inferred to have been low, certainly less than the creep and fracture strengths of feldspar at the ambient pressure, temperature and strain rate of deformation.

Handy (1990) has shown that at high shear strains, a crude foliation comprising elongate clusters of strong grains develops parallel to the shearing plane (see his fig. 2b). The greater the aspect ratio of the strong grain clusters, the lower the stress concentration in the matrix and the more nearly uniform the stress distribution within the aggregate (Handy 1992). This raises the basic question of whether the IWL microstructure is a steady-state configuration or whether it only represents an intermediate stage in a continuous evolution towards perfect interconnectivity of both phases.

There is convincing evidence that the IWL microstructure is indeed a steady-state configuration: shearing of perfectly layered, viscous materials leads to boudinage of the stronger layers and coalescence of the weak layers (e.g. fig. 1.8 in Ramsay & Huber 1987). Perfectly layered materials are therefore unstable with respect to the IWL structure. Likewise, two-phase aggregates with a LBF microstructure are unstable over a broad range of compositions and breakdown to an IWL microstructure (Jordan 1988, Handy 1990, discussions below). Means (1981) cites the cyclic growth and destruction of microstructural elements as diagnostic of steady-state foliations. In the quartzite mylonite in Fig. 2, the boudinaged ribbon and globular grains are inferred to have coalesced from smaller protograins preserved in less deformed rock outside of the shear zone (fig. 8 in Handy 1987). Means & Dong (1982) and Urai *et al.* (1986) present microstructural evidence for the cyclic growth and dynamic recrystallization of ribbon grains during mylonitization. Similarly, the interconnected layers of dynamically recrystallized quartz in Fig. 2 contain the entire spectrum of grain sizes and shapes, from small, equant, freshly nucleated grains to larger, elongate older grains. Strain-invariance is an important characteristic of the IWL microstructure because it means that stress and strain rate partitioning within the aggregate can be related to steady-state bulk rheology.

*Inferred stress and strain rate partitioning across rheological interfaces*

Based on the piezometric measurements above, inferred stress and strain rate profiles across the interface between weak and strong phases in IWL and LBF microstructures are drawn schematically in Fig. 5. Each diagram in Fig. 5 includes two sets of solid vertical lines representing the relative levels of stress and strain rate for the limiting cases of homogeneous stress and homogeneous strain rate within the polyphase aggregate.

For rock with IWL structure, one might expect the stresses and strain rates of the constituent phases always to fall between the uniform stress and uniform strain rate bounds (hatched areas, Fig. 5a). According to the bounding theorems approach, the highest possible stress and strain rate in the weak phase occur when both phases are interconnected and deform at the same stress on either side of a coherent interface (curve 1, Fig. 5a). In nature, however, only the weak phase is interconnected and slip along incoherent phase boundaries maintains strain compatibility within the aggregate. As shown in the previous section, this condition can lead to higher stress in the weak layers than in the strong boudins. This accords with continuum mechanical models that predict reduced flow stress in boudinaged layers and concomitant stress concentration in the adjacent incompetent layers subparallel to the shearing plane (Strömgård 1973, Weijermars 1991). Because viscous flow is isochoric and the deformation is compatible, the weak phase is inferred to deform at a higher average stress and strain rate than at the uniform stress bound (curve 3, Fig. 5a). Conversely, the stronger phase deforms at a lower average stress and strain rate than at this

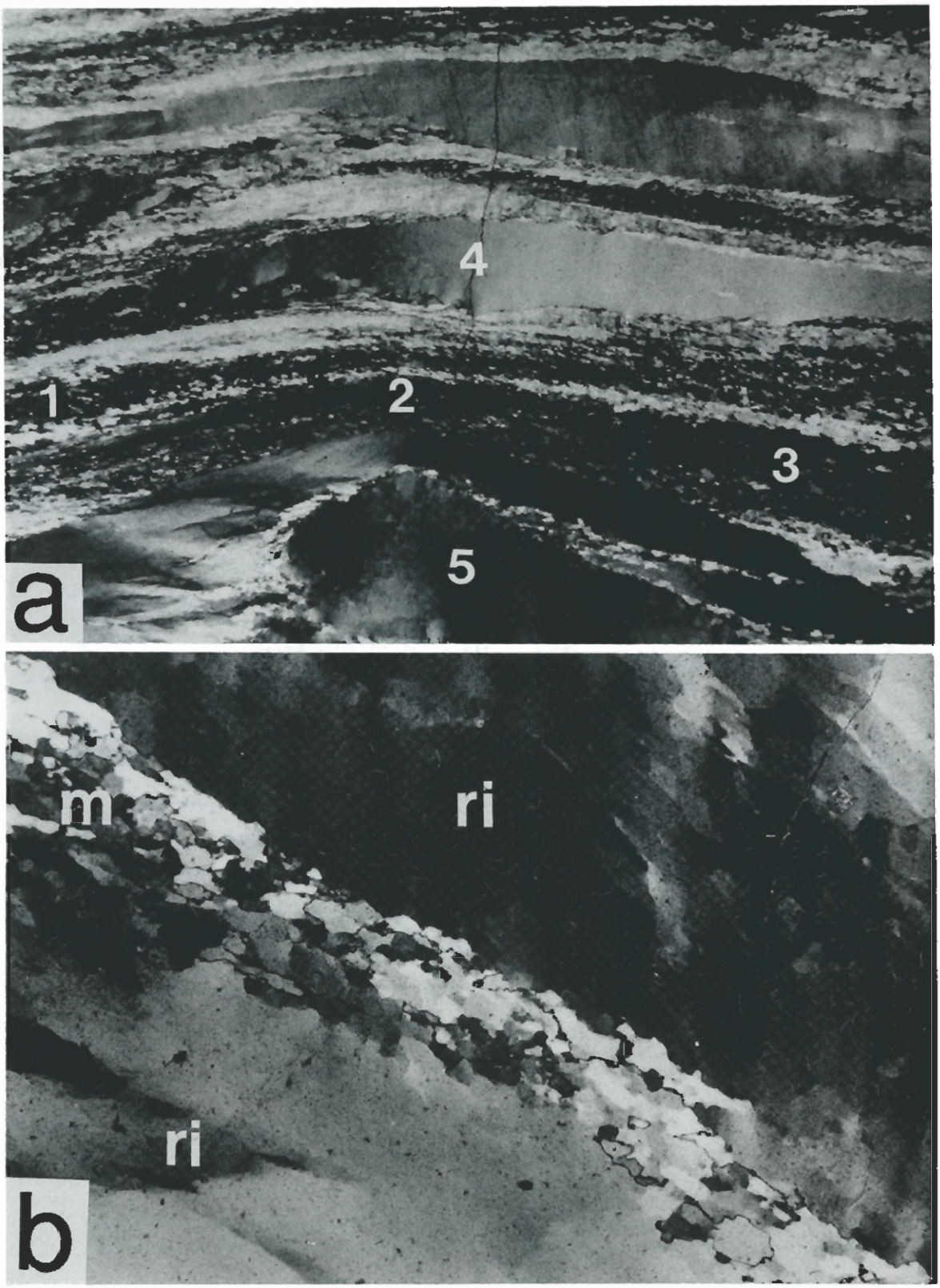


Fig. 2. (a)Heterogeneously deformed quartz mylonite comprising an interconnected matrix of dynamically recrystallized grains (e.g. areas 1–3) surrounding unrecrystallized ribbon (e.g. area 4) and globular grains (area 5). Numbers correspond to areas in which stress-dependent grain size was measured (see Fig. 4). Section cut parallel to $XZ$ fabric plane. Crossed polarizers, frame dimensions: 11.5 × 7.7 mm. (b) Subgrains at the interface between ribbon grains (ri) and dynamically recrystallized matrix (m) in quartz mylonite. Crossed polarizers, frame dimensions: 1.4 × 1.0 mm.

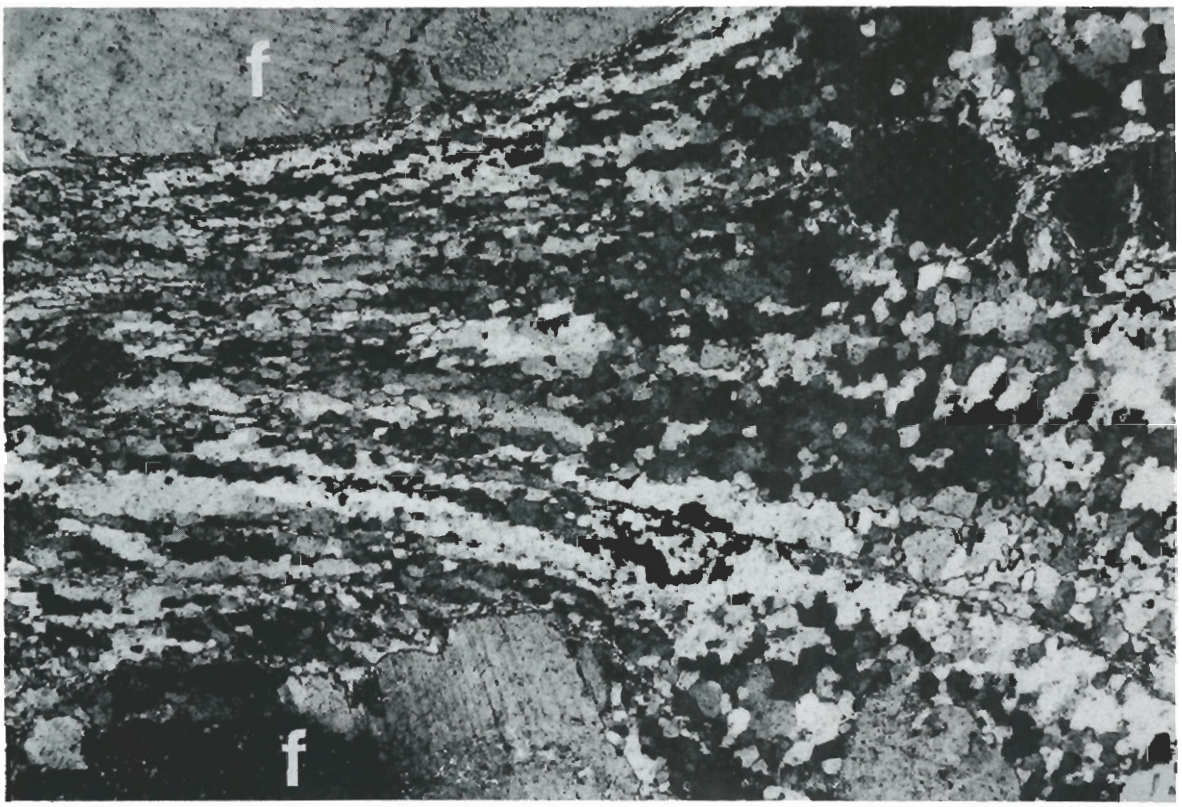


Fig. 3. Dynamically recrystallized quartz between two feldspar grains (labelled f) in a greenschist facies mylonite. Section cut parallel to $XZ$ fabric plane. Crossed polarizers, frame dimensions: 1.4 × 1.0 mm.

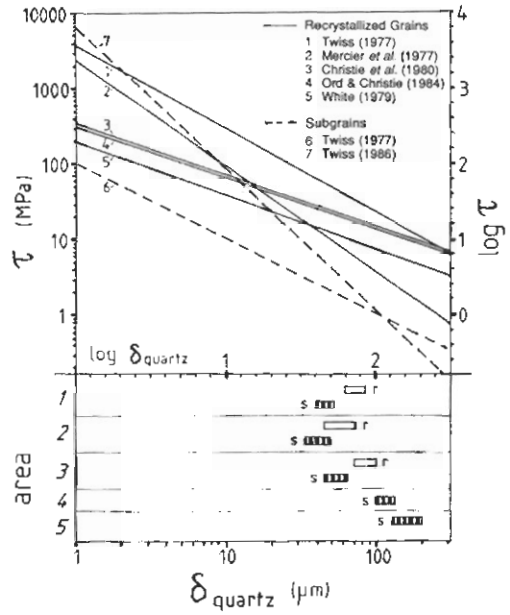


Fig. 4. Plot of creep stress vs dynamically recrystallized grain size (r) and subgrain size (s) for quartz in the various microstructural areas numbered in Fig. 2(a). Length of grain size bars indicates population standard deviation of grain size.

bound. Two conditions are expected to promote such stress partitioning: (1) the rock comprises small to moderate amounts of weak phase; and/or (2) the stress dependence of strain rate in the strong phase significantly exceeds that in the weak phase (i.e. high ratios of the creep exponents, $n_s/n_w$). For rock containing greater volume proportions of weak phase and/or phases with lower $n_s/n_w$ ratios, the stress in the strong boudins exceeds that in the weak layers at most bulk strain rates and two-phase compositions (curve 4, Fig. 5a). Generally, the partitioning of stress and strain rate as well as the amount of interfacial slip between the phases becomes more pronounced with increased mineral strength contrast and/or with decreased volume proportions of incompetent material.

The LBF structure is rarely observed or identified in highly strained rock (see fig. 2a in Handy 1990 for a low strain example). This is due partly to the ambiguous criteria for distinguishing strong from weak boudinaged layers in IWL and LBF structures, particularly at low mineral strength contrasts (Fig. 1). It may also reflect the inherent instability of the LBF structure at high strains and moderate to high volume proportions of weak phase (Handy 1990 and below). So unfortunately, no natural example of an LBF structure with stress dependent microstructures could be analysed here. However, Treagus & Sokoutis (1992) have shown that non-linear composite silicon materials with low mineral strength contrast ($\tau_c = 1.66$) in an LBF structure deform at nearly uniform shear strain rate to strains of $\gamma = 1.15$ in a simple shear box (see their figs. 5b and 9b, curve 2 in Fig. 5b of this paper). Deviations from homogeneous strain rate occur in the immediate vicinity of the phase boundaries. This is because weak and strong phases are constrained to deform both compatibly and at similar rates within the load bearing framework, thus inducing large differential stresses at these boundaries. These localized differential stresses are relaxed somewhat if the phases slip with respect to each other. The nature of this slip, as well as the stresses and strain rates at the phase boundaries depend on strain-dependent changes in the configuration of the weak pockets.

In the absence of detailed studies of LBF microstructures, it is useful to draw an analogy between the microstructural evolution of porous polycrystalline aggregates (e.g. Ashby *et al.* 1979) and rocks with an LBF microstructure. Similar to voids or cavities in porous plastic aggregates, the pockets of weak phase are inferred to become more elongate with progressive strain until either: (1) their shape stabilizes within limits corresponding to cyclic growth and boudinage at steady state; or (2) their growth becomes unstable and they coalesce to form interconnected weak layers. At steady state (case 1), pocket growth involving high strain rate in the weak phase alternates with pocket boudinage involving high strain rate in the adjacent strong framework (curves 5 and 6 in Fig. 5b). Cyclic growth and boudinage go on simultaneously within the LBF microstructure, so that the rock as a whole still deforms at or near uniform strain rate. The coalescence of weak pockets is inhibited by dynamic recrystallization in the strong phase of the LBF microstructure, which facilitates rapid ductile flow and stress relief in the neck regions between pockets (Ashby *et al.* 1979). Creep instabilities are generally suppressed in rock comprising a strong phase with low stress sensitivity (i.e. low values of the creep exponent, $n$) and/or phases with similar bulk and shear moduli. In case (2) above, weak pockets coalesce when the stress

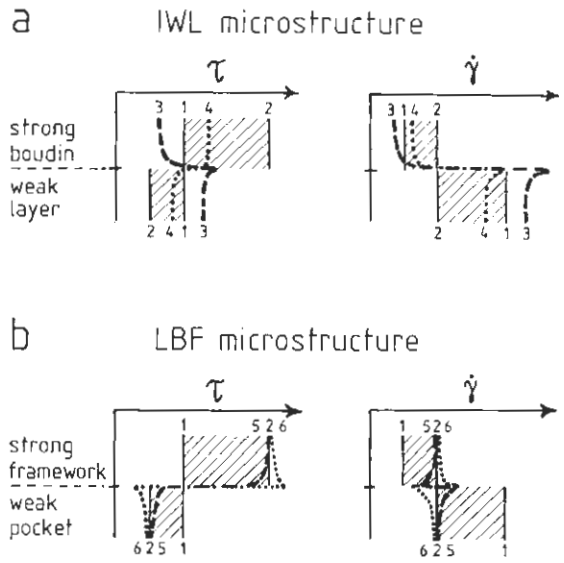


Fig. 5. Schematic profiles of shear stress and shear strain rate across a rheological interface within a viscous composite material at steady-state comprising: (a) an IWL microstructure; and (b) an LBF microstructure. Hatched area contains stresses and strain rates between bounds for uniform stress (curve 1) and uniform strain rate (curve 2). Dashed and dotted curves in (a) are inferred stresses and strain rates in an IWL microstructure bearing constituent phases with high $n_s/n_w$ ratios (curve 3) and low $n_s/n_w$ ratios (curve 4). Dashed and dotted curves in (b) represent inferred stress and strain rate in an LBF microstructure during cyclic growth (curve 5) and boudinage (curve 6) of weak products at steady state (see text).

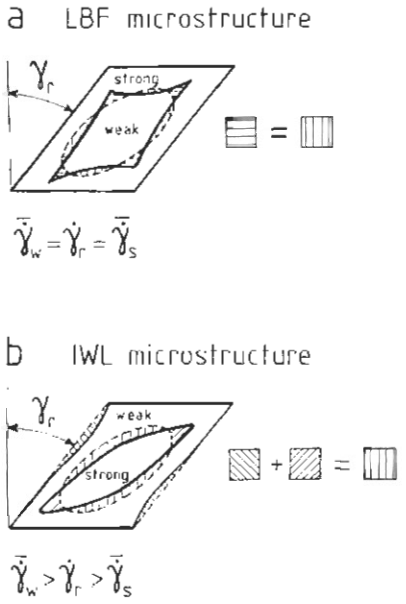


Fig. 6. Microstructures modelled in this paper for rocks with a load-bearing framework (LBF) and interconnected weak layers (IWL) undergoing plane strain, simple shear. Strain compatibility is depicted schematically as the balance of gaps and overlaps (hatched areas) produced by the heterogeneous deformation and rotation of inclusions during progressive simple shear. Dashed lines indicate configuration of phase boundaries for the ideal case of plane strain, homogeneous simple shear.

concentration at the pocket tips becomes sufficiently large to induce unstable flow in the neck regions between elongate weak pockets, causing the pockets to propagate like tensile microcracks (Griffith *et al.* 1979). In contrast to voids, however, the weak pockets have finite values of the bulk and shear moduli. For a given strain, weak pockets are therefore expected to remain stable to higher volume proportions of weak phase and/or to require greater strain to coalesce than voids.

A significant point to emerge from the microstructural analyses above is that the stress contrast of two phases within a composite material differs considerably from their strength (i.e. competence) contrast. Strength contrast depends on the material parameters of the constituent phases and on the bulk strain rate, temperature and pressure, whereas stress contrast varies with the strength contrast, the volume proportions, and the distribution of the phases in the composite. This distinction becomes important in the next section.

## PHENOMENOLOGICAL FLOW LAWS FOR NON-LINEAR VISCOUS TWO-PHASE MATERIALS

### *General conditions and assumptions*

Consider a hypothetical two-phase rock undergoing plane-strain, simple shear at constant bulk shear strain rate, $\dot{\gamma}_r$. The volume proportions of the two minerals in the rock remain constant with strain. These phases form a steady-state foliation (Means 1981) that is aligned subparallel to the plane of shear. In an ideal LBF microstructure (Fig. 6a), this foliation comprises a strong phase containing a pocket of weak phase, whereas in an ideal IWL microstructure the foliation consists of a weak matrix surrounding a stronger phase (Fig. 6b). In both microstructures, all mineral phases in the rock are viscous isotropic materials that deform compatibly and isochorically by dislocation creep. Any dilatancy within, or mass-transfer between, the phases is assumed to be negligible. Note that for the strain to be compatible in the LBF and IWL microstructures in Fig. 6, the phases must deform heterogeneously and their boundaries must accommodate slip. This is especially true of rock with IWL structure that contains large volume proportions of a relatively strong phase undergoing noncoaxial flow to high shear strains.

A key to deriving the polyphase flow laws in the next section is the notion that *the rate of viscous strain energy dissipation in a rock is equal to the sum of the effective rates of strain energy dissipation in the constituent phases of that rock*:

$$\dot{E}_r V_r = \sum_{i=1}^{N} \tau_i \dot{\gamma}_i V_i, \tag{2}$$

where the rate of viscous shear strain energy or power dissipated in a rock, $\dot{E}_r$, of volume $V_r$ is equal to the sum of the inner products of the shear stress and incremental shear strain rate tensors, $\tau_i$ and $\dot{\gamma}_i$, and the volume, $V_i$, of each of the $N$ constituent phases, $i$. For the two-phase aggregate considered in this paper, equation (2) simplifies to:

$$\dot{E}_r = \tau_w \dot{\gamma}_w \phi_w + \tau_s \dot{\gamma}_s \phi_s, \tag{3}$$

where $\dot{\gamma}_w$ and $\dot{\gamma}_s$ are the octahedral shear strain rates of the weak and strong phases, $\tau_w$ and $\tau_s$ are the corresponding octahedral shear stresses in these phases, and where $\phi_w$ and $\phi_s$ are the volume proportions of weak and strong phases in the two-phase rock. The volume of the whole rock is set equal to one, so that the volume proportions of the phases sum to unity, $\phi_w + \phi_s = 1$. Equations (2) and (3) are actually adaptations of Einstein's (1909, 1911) concept of viscous energy dissipation in slowly deforming, viscous suspensions containing rigid spheres. In this context, it is important to point out that shearing of the rock is assumed to be isothermal. The viscous strain energy is dissipated quickly enough to avoid shear-heating and any feedback effects this might have on the rheology (Hobbs & Ord 1988) or chemical stability (e.g. Rutter & Brodie 1987) of the phases making up the rock.

Because flow of the hypothetical rock is isochoric and strain compatibility is maintained amongst the constituent phases (Fig. 6), *the effective* (*i.e. volume-weighted*) *average strain rates of the weak and strong phases are additive* in both LBF and IWL microstructures:

$$\dot{\gamma}_r = \bar{\dot{\gamma}}_w \phi_w + \bar{\dot{\gamma}}_s \phi_s, \tag{4}$$

where $\bar{\dot{\gamma}}_w$ and $\bar{\dot{\gamma}}_s$ are the averaged octahedral shear strain rates of the weak and strong phases, respectively, and where $\phi_w$ and $\phi_s$ have been defined above. This relation is important in two respects: first, it allows the average

strain rate of a phase to be calculated if the bulk strain rate, the volume proportions of phases, and the average strain rate of the remaining phase are known (equation 9 below); second, because slip is allowed between the phases equation (4) implies that the average stress in the two phases can differ. This condition pertains especially to the IWL microstructure.

Strain rate is related solely to the differential creep stress in the rock because inertial forces are negligible at the slow, natural strain rates considered here ($10^{-9}$–$10^{-15}$ $s^{-1}$). Therefore, the empirically derived constitutive equation for creep relating shear stress to shear strain rate in the constituent phases in equations (3) and (4) is (after Weertman 1968):

$$\tau_i = \exp\left(\frac{1}{n_i}\left\{\frac{Q_i}{RT} + \ln\left[\frac{\bar{\dot{\gamma}}_i}{3^{(n_i+1)/2}A_i}\right]\right\}\right), \qquad (5)$$

where $\bar{\dot{\gamma}}_i$ is the average shear strain rate in the $i$-th phase at temperature $T$, $Q_i$ is the activation enthalpy of creep, $n_i$ is the creep exponent and $A_i$ is a pre-exponential function. The factor $3^{(n+1)/2}$ (Nye 1953, Stocker & Ashby 1973, Schmid *et al.* 1987) converts the stress and strain rate tensors from the pure shear configuration of the triaxial experiments to the plane-strain simple (octahedral) shear configuration assumed here. The value of $\tau_i$ obtained at an average shear strain rate in equation (5) slightly exceeds the average shear stress because of the non-linear relationship between stress and strain rate in minerals undergoing dislocation creep ($n > 1$ in equation 5). This discrepancy in stress values is greater at low strain rates and for materials with large creep exponents. Inaccuracies in stress estimates arising from the assumption of average strain rate for the constituent phases are discussed at the end of the next section.

### *Deriving composite flow laws for rocks with ideal LBF and IWL microstructures*

In a rock deforming at steady state with an ideal LBF microstructure, the load-bearing framework of strong phase forces the pockets of weak phase to strain at the same rate, regardless of any rheological contrast between the phases (Fig. 6a). The experiments of Treagus & Sokoutis (1992) reviewed above indicate that deviations from uniform strain rate are very small, justifying the simple assumption that the average strain rate of the constituent phases is uniform and equals the strain rate of the rock. Therefore, the viscous shear strength of a two-phase rock with an LBF microstructure, $\tau_r^{LBF}$, is obtained by substituting the bulk shear strain rate into all strain rate terms in equation (3), then dividing the resultant power dissipation for the whole rock by the same bulk shear strain rate. This yields the familiar upper bound strength of polyphase rocks:

$$\tau_r^{LBF} = \tau_{wr}\phi_w + \tau_{sr}\phi_s, \qquad (6)$$

where $\tau_{wr}$ and $\tau_{sr}$ are the octahedral shear stresses in weak and strong phases at temperature, $T$, and at the overall shear strain rate of the rock, $\dot{\gamma}_r$. The strain energy approach used here to obtain equation (6) for a rock with LBF structure contrasts with past derivations of this equation which employ a continuum mechanics approach and assume that both phases are contiguous within the shearing plane (e.g. Weijermars 1992).

Deriving a steady-state constitutive equation for rocks with an ideal IWL microstructure (Fig. 6b) is more difficult because stress and strain rate partitioning in the aggregate depends on the viscous strength contrast between the constituent phases, as well as on the relative amounts of these phases. The viscous shear strength contrast, $\tau_c$, is defined here as:

$$\tau_c = \frac{\tau_{sr}}{\tau_{wr}}, \qquad (7)$$

where $\tau_{sr}$ and $\tau_{wr}$ are the octahedral shear stresses in the strong and weak phases measured separately (i.e. outside the aggregate) at temperature, $T$, and at a reference shear strain rate that equals the overall shear strain rate of the aggregate, $\dot{\gamma}_r$. The dependence of stress and strain rate partitioning on $\tau_c$ is constrained by considering the following limiting conditions from the microstructural observations in the previous section:

(a) As the viscous strength contrast of the phases becomes infinite, the bulk strain rate is concentrated into the volume of rock comprising the weaker phases, while the average strain rate of the stronger phase approaches zero:

$$\bar{\dot{\gamma}}_w \to \dot{\gamma}_r\phi_w^{-1}, \qquad \bar{\dot{\gamma}}_s \to 0,$$

where

$$0 < \phi_w < 1.$$

(b) If the viscous strength of the two phases is equal, then the strain rate of the rock is equal to the strain rate in both phases (homogeneous deformation) for all volume proportions of strong and weak phases:

$$\bar{\dot{\gamma}}_w = \bar{\dot{\gamma}}_s = \dot{\gamma}_r \quad \text{at} \quad 0 < \phi_w < 1.$$

These constraints are now used to seek an expression that describes how the average strain rate in the weak phase varies with the strain rate of the rock, and with both the volume proportions and the viscous strength contrast of the two constituent phases. This expression has a form similar to the limit in condition (a) above:

$$\bar{\dot{\gamma}}_w = \dot{\gamma}_r\phi_w^{-x}, \qquad (8)$$

where $x$ is a function of $\tau_c$ for $1 \leq \tau_c \leq \infty$. The function $x$, here named the strain rate concentration function, is a measure of the $\tau_c$-sensitivity of strain rate partitioning in the rock. Specifically, it determines how much of the total strain rate is accommodated by the volume of weak phase. An expression analogous to equation (8) for the average strain rate of the strong phase is obtained by substituting equation (8) into equation (4) and solving for $\bar{\dot{\gamma}}_s$:

$$\bar{\dot{\gamma}}_s = \dot{\gamma}_r(1 - \phi_w)^{-1}(1 - \phi_w^{1-x}). \qquad (9)$$

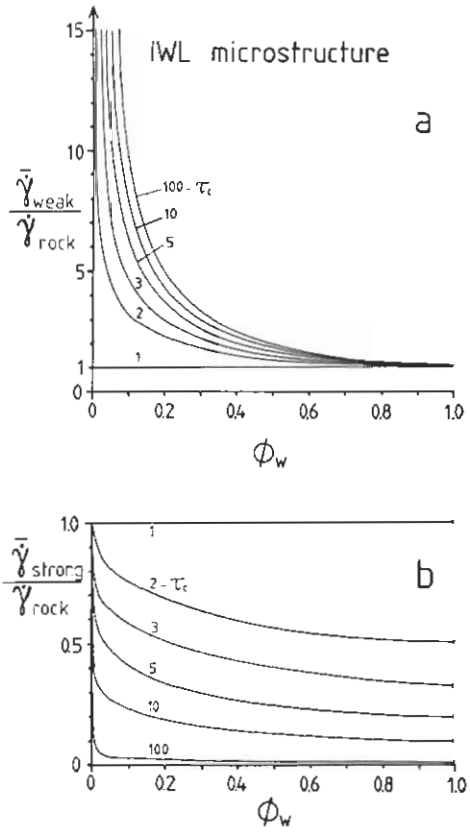


Fig. 7. Strain rate concentration vs volume proportion of weak phase in two-phase aggregates with an IWL microstructure. (a) is a plot of equation (8), (b) is a plot of equation (9). Both equations incorporate the function $x = (1 - 1/\tau_c)$ in equation (10), allowing the diagrams to be contoured for different values of the viscous strength contrast, $\tau_c$.

The $\tau_c$-dependence of $x$ in equations (8) and (9) can be constrained in the following way: (1) $0 \leq x \leq 1$ for $0 < \phi_w < 1$ (conditions a and b); (2) $x \rightarrow 1$ as $\tau_c \rightarrow \infty$ (condition a); (3) $x \rightarrow 0$ as $\tau_c \rightarrow 1$ (condition b). The simplest expression of $x$ that is a smooth function of $\tau_c$ and that satisfies all the constraints above is:

$$x = 1 - \frac{1}{\tau_c} \quad \text{when } 0 < \phi_w < 1. \tag{10}$$

In monomineralic rocks, $x$ is undefined and so obviously $\bar{\dot{\gamma}}_w = \dot{\gamma}_r$ at $\phi_w = 1$ and $\bar{\dot{\gamma}}_s = \dot{\gamma}_r$ at $\phi_w = 0$. Although equation (10) is certainly not a unique solution to the constraints above, this writer could find no constraints for values of $\tau_c$ between 1 and $\infty$ to warrant the use of a more complicated function for $x$. Despite this limitation, equation (10) provides a reasonable approximation of the $\tau_c$-sensitivity of strain rate partitioning in two-phase aggregates (see next section).

Figures 7(a) & (b) furnish a direct demonstration of equations (8) and (9), respectively, for varied strength contrasts of the constituent phases in a hypothetical two-phase rock. They illustrate the physical significance of the strain rate concentration factor, $x$, in equation (10). The concentration of average strain rate and creep stress into the weaker phase of a rock with IWL microstructure increases with decreasing abundance of that phase and/or with increasing viscous strength contrast between the two phases (Fig. 7a). Conversely, the average strain rate of the strong phase decreases with decreasing abundance of that phase and increasing strength contrast between the phases (Fig. 7b). Figure 7(a) also indicates that the average strain rate (and therefore also stress) in the interconnected weak phase of an IWL structure rises to infinity at sufficiently low values of $\phi_w$. This is geologically unrealistic because creep stress cannot exceed the brittle strength of the material. In this paper, it is proposed that the upper limits to the stress and strain rate in the interconnected weak phase coincide with a balance in the rate of strain energy dissipated by the LBF and IWL structures at equal bulk strain rate and temperature. This criterion for structural stability is discussed further below.

The rate of viscous shear strain energy dissipated in a rock with an IWL microstructure, $\dot{E}_r^{IWL}$, is obtained by substituting equations (8) and (9) into all the strain rate terms in equation (3). Dividing the resultant $\dot{E}_r^{IWL}$ by $\dot{\gamma}_r$ yields the viscous shear strength of a rock with an IWL microstructure, $\tau_r^{IWL}$:

$$\tau_r^{IWL} = \tau_w \phi_w^{1-x} + \tau_s \underbrace{\qquad\qquad}_{(1 - \phi_w^{1-x})}, \tag{11}$$

where $\tau_w$ and $\tau_s$ are the octahedral shear stresses in the weak and strong phases, respectively, at $\dot{\gamma}_w$ and $\dot{\gamma}_s$ and at given $\phi_w$.

To summarize this section, equations (6) and (11) express the steady-state viscous strength of two-phase rocks with LBF and IWL microstructures solely in terms of the bulk strain rate, the temperature, the volume proportions of the constituent phases, and the rheological constants of these phases. The microstructure with the lower overall rate of viscous strain energy dissipation in equation (3) is the configuration expected to remain stable in a rock deforming at a given temperature and strain rate.

## COMPARISON OF THEORETICAL FLOW LAWS WITH COMPUTED AND EXPERIMENTAL RHEOLOGIES OF BIMINERALIC ROCK

Currently, only two experiments on bimineralic aggregates from the literature can be compared with the flow laws in equations (6) and (11): (1) the finite element simulation of creep in plagioclase–clinopyroxene aggregates (Tullis *et al.* 1991); and (2) the laboratory deformation of diabase (Shelton & Tullis 1981) at mineral strength contrasts of 4 and less. These experiments were chosen because both phases in the aggregates deformed by dislocation creep and their rheologies are well known. Use of these data also facilitates a direct comparison of the two-phase flow laws proposed in this paper with the empirically derived flow law of Tullis *et al.* (1991). Unfortunately, bimineralic aggregates with higher viscous strength contrasts (Price 1982, Jordan 1987) contain strong phases that deformed cataclastically and their strength–composition data are therefore unsuited for comparison with the theoretical flow laws in this paper.

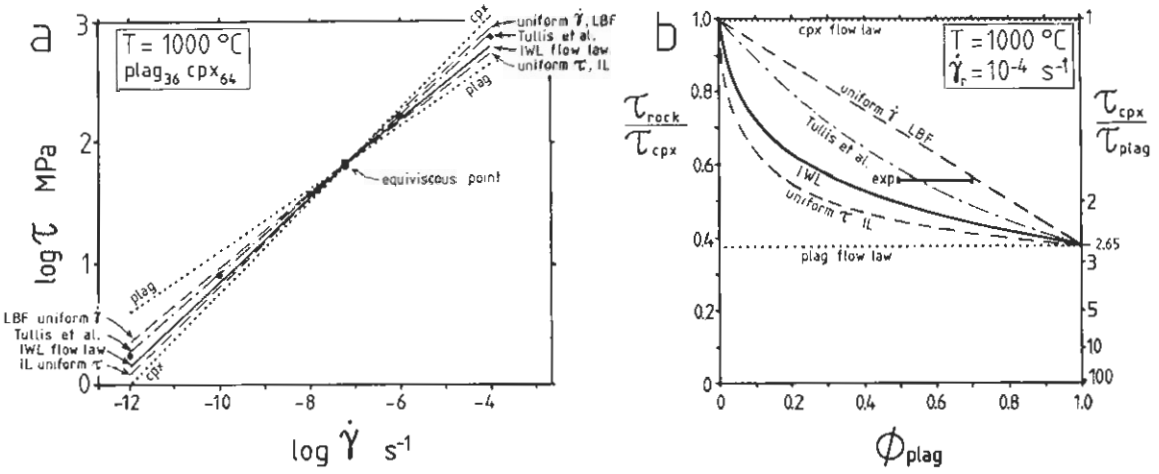


Fig. 8. (a) Log shear strain (MPa) vs log shear strain rate ($s^{-1}$) diagram for a hydrous clinopyroxene–plagioclase aggregate. Extrapolated end-member flow laws (dotted curves), uniform stress and uniform strain rate bounds (dashed curves), IWL flow law for cpx–plag rock from equation (11) in this paper (solid curve), empirical flow law for diabase of Tullis *et al.* (1991) (dashed–dotted curve), computer-simulated strengths for deformed diabase (grid 3 of Tullis *et al.* 1991) (large dots). Rheological parameters for constituent phases are taken from experiments of Shelton & Tullis (1981) performed at 1000°C and $10^{-4}$ $s^{-1}$: albitic plagioclase: $n = 3.9$, $Q = 234$ kJ $m^{-1}$, $A = 2.51 \times 10^{-6}$ $MPa^{-n}$ $s^{-1}$; clinopyroxene: $n = 2.6$, $Q = 335$ kJ $m^{-1}$, $A = 15.85$ $MPa^{-n}$ $s^{-1}$. (b) Plot of normalized shear stress vs volume proportion of plagioclase for hydrous plagioclase–clinopyroxene aggregates. Uniform stress and uniform strain rate bounds (dashed curves), theoretical flow law for cpx–plag rock with IWL microstructure from equation (11) in this paper (thick solid curve), empirical flow law of Tullis *et al.* (1991) (dashed–dotted curve), experimentally determined flow law for Maryland diabase from Shelton & Tullis (1981) (thick horizontal line). Note that this diagram is constructed for the same conditions as used by Shelton & Tullis (1981) to determine the flow laws of the constituent phases. Creep parameters for the plagioclase and clinopyroxene end-members are identical to those in (a). Creep parameters for Maryland diabase determined at 1000°C and $10^{-4}$ $s^{-1}$ (Shelton & Tullis 1981): $n = 3.4$, $Q = 259$ kJ $m^{-1}$, $A = 2 \times 10^{-4}$ $MPa^{-n}$ $s^{-1}$.

The stress vs strain rate diagram in Fig. 8(a) compares the synthetically computed and theoretically predicted creep stresses for a foliated diabase containing 36 vol.% plagioclase and 64 vol.% clinopyroxene, and deforming at a temperature of 1000°C with bulk shear strain rate ranging from $10^{-4}$ to $10^{-12}$ $s^{-1}$. At these conditions, the shear strength ratio between plagioclase and clinopyroxene varies from 4 (plag stronger than cpx, $\dot{\gamma}_r = 10^{-4}$ $s^{-1}$ through 1 (equiviscous point in Fig. 8a) to 2.65 (cpx stronger than plag, $\dot{\gamma}_r = 10^{-12}$ $s^{-1}$). Both phases are highly contiguous in the foliation plane, with plagioclase slightly more interconnected than clinopyroxene (see fig. 1b of grid 3 in Tullis *et al.* 1991). Figure 8(a) shows that the rock strength predicted with the IWL flow law (solid line) lies well within the strengths derived from the extrapolated end-member flow laws (dotted lines) and the uniform stress and uniform strain rate bounds (dashed lines) over the complete range of natural to simulated strain rates. However, the IWL flow law predicts consistently lower strengths for diabase than does the finite element simulation of Tullis *et al.* (1991).

The normalized rock strength vs composition diagram in Fig. 8(b) is constructed with the same flow laws as in Fig. 8(a) for a bulk shear strain rate of $\dot{\gamma}_r = 10^{-4}$ $s^{-1}$. Normalized strength on the left-hand axis of Fig. 8(b) is merely the strength of the rock normalized to the strength of the stronger phase (the strength of clinopyroxene is set equal to 1) and scaled against the strength contrast, $\tau_c$, of clinopyroxene to plagioclase on the right-hand axis. The strength for rocks with the ideal LBF, uniform strain rate flow law and the IWL flow law bracket the experimental creep strength of Maryland diabase at $\dot{\gamma}_r = 10^{-4}$ $s^{-1}$ (horizontal bar in Fig. 8b). For comparison, the empirical flow law of Tullis *et al.* (1991) calculated with their equations (10)–(12) is an excellent fit both to the experimental diabase strength (Fig. 8b) and to their computer-simulated diabase strengths across the entire range of strain rates and bimineralic compositions (dashed–dotted curve, Figs. 8a & b).

The ideal LBF, uniform strain rate flow law clearly overestimates experimental and computer-simulated diabase strengths because both plagioclase and clinopyroxene constitute lenticular layers within the foliation plane. There are two main reasons why the IWL flow law underestimates the experimental and computer-simulated diabase strengths: (1) the $\tau_c$-dependence of the strain rate concentration function, $x$, may be less than that derived using the available constraints in equation (10); (2) the use of average strain rates in equations (8) and (9) neglects the effect of localized stress concentration on bulk rock strength. Where layers of weak phase are constricted between stronger phases (e.g. Fig. 3), creep stress and strain rate rise non-linearly above ambient levels in the IWL microstructure (Handy 1990, 1992). This effect becomes more pronounced with increasing $\tau_c$ and increasing amounts of strong phase in the rock.

In summary, two-phase rock strength predicted with equation (11) for an IWL microstructure is closer to the uniform stress bound than to the uniform strain rate bound over a broad range of compositions. In aggregates with low mineral strength contrasts ($\tau_c \leq 4$) and/or with low volume proportions of a weak phase ($\phi_w < 0.1$), the aggregate strength approaches the uniform strain rate bound for an ideal LBF microstructure (equation 6).

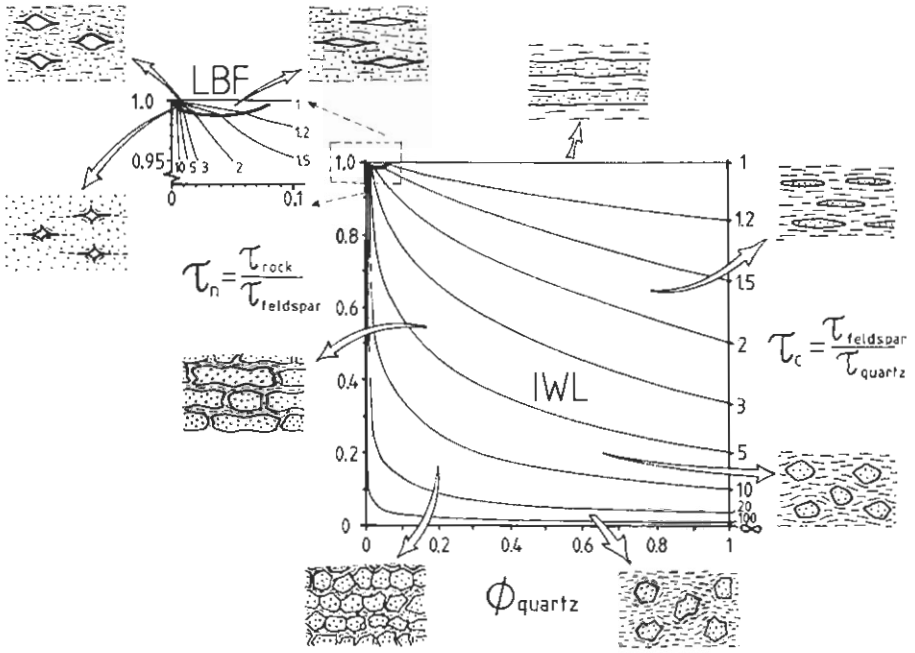


Fig. 9. Structural stability diagram for quartz–feldspar rock. Rock strength on the left-hand axis is normalized to the viscous strength of feldspar (strength of feldspar is set equal to 1). Viscous strength ratio of feldspar to quartz increases downwards on the right-hand axis. The thick curve marks the boundary between the LBF and IWL fields. The thin curves are contours of normalized rock strength at different values of mineral strength contrast, $\tau_c$. Microstructural insets depict the steady-state configuration of strong phase (stippled), weak phase (white) and flow lines (dashes). Creep parameters of the hydrous end-member phases: quartzite: $n = 2.4$, $Q = 163$ kJ m$^{-1}$, $A = 10^{-5}$ MPa$^{-n}$ s$^{-1}$ (Jaoul *et al.* 1984); albitic plagioclase: $n = 3.9$, $Q = 234$ kJ m$^{-1}$, $A = 2.51 \times 10^{-6}$ MPa$^{-n}$ s$^{-1}$ (Shelton & Tullis 1981).

## IMPLICATIONS FOR THE RHEOLOGY AND MICROSTRUCTURE OF POLYMINERALIC ROCKS

Figure 9 is a structural stability diagram for quartz–feldspar rock spanning the compositional range from diorite, through granite, to quartzite. It contains LBF and IWL fields contoured for normalized rock strength at different mineral strength contrasts. The microstructural insets in Fig. 9 show how steady-state polyphase configuration varies within the diagram as a function of composition and mineral strength contrast.

Diagrams like Fig. 9 can be constructed for any two-phase aggregate with equations (6) and (11). The boundary between the LBF and IWL fields is the locus of points at given values of $\phi_w$, $\dot{\gamma}_r$, and temperature where, according to these equations, both microstructures yield the same bulk strength and so dissipate identical amounts of strain energy per unit time. On either side of the LBF–IWL boundary, the more stable microstructure is assumed to be that configuration which is weaker at a given $\dot{\gamma}_r$ and therefore dissipates less strain energy per unit time during steady-state deformation. Each contour of normalized rock strength at a constant mineral strength contrast is determined for a given temperature and bulk shear strain rate in equations (6) (LBF field) and (11) (IWL field).

The IWL microstructure is predicted to be more stable than the LBF microstructure during steady-state flow over a broad range of compositions and viscous strength contrasts between the constituent phases (Fig. 9). This is consistent with the observation that the IWL microstructure is much more common than the LBF microstructure in highly strained rocks, even at low $\phi_w$ values. The critical volume proportion of weak phase at the boundary between the LBF and IWL microstructural stability fields depends on the mineral strength contrast (see detailed inset, Fig. 9). This is a function of both the creep parameters of the constituent phases and the temperature and bulk strain rate of deformation. For given temperature and bulk strain rate, low ratios of the creep activation energies ($Q_s/Q_w < 1.5$) and high ratios of the creep exponents ($n_s/n_w > 1$) expand the stability field of the LBF microstructure to values of $\phi_w \geq 0.1$ in Fig. 9. Moderate to large $Q_s/Q_w$ ratios (>1.5) and low $n_s/n_w$ ratios (<1) restrict the LBF microstructure to values of $\phi_w \ll 0.1$ in the upper left-hand corner of Fig. 9.

The contours in the LBF field of Fig. 9 indicate a nearly linear dependence of normalized aggregate strength on two-phase composition at low $\phi_w$ values, whereas the contours in the IWL field are highly nonlinear, especially at high mineral strength contrasts and low $\phi_w$ values. While this obviously reflects the assumptions made in equations (6) and (11), it is also intuitively reasonable: If strong phase could be added to a rock comprising two phases at given $\tau_c$, the rate of work would increase more rapidly in a rock with IWL microstructure where the interconnected weak phase deforms much faster than the strong phase, than in a rock with LBF microstructure where the pockets of weak phase deform at same rate as the framework of strong phase.

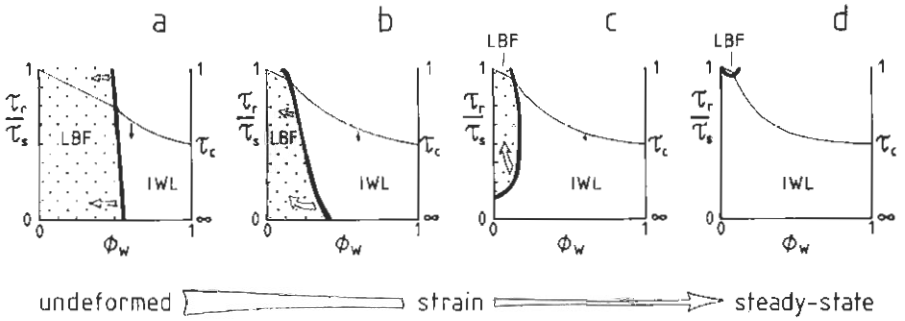


Fig. 10. Inferred strain-dependent evolution of the LBF and IWL fields in a schematic structural stability diagram: (a) undeformed state; (b) low strain stage typically achieved in triaxial experiments; (c) intermediate strain stage; and (d) steady state. Arrows indicate the strain-dependent movement of the LBF–IWL boundary (thick curve) and a contour of normalized rock strength at constant $\tau_c$ (thin curve).

The difference in the strain rates of the weak phase in the two microstructures grows with increasing viscous strength contrast between the phases (recall Fig. 7).

The hypothesis of strain energy minimization employed above to distinguish fields of microstructural stability during steady-state creep only compares end-member states of power dissipation for LBF and IWL microstructures. It does not describe the structural and mechanical changes leading to these states. Figure 10 is a qualitative attempt to illustrate this evolution based partly on insight from experimental triaxial deformation of two-phase aggregates and partly on inference. In the unstrained state (Fig. 10a), the configuration of the LBF and IWL fields reflects the geometry and distribution of phases in the rock, and therefore also mirrors the rock's previous geologic history. As drawn in Fig. 10(a), the broad LBF field betrays extensive contiguity of the strong phase, such as might occur in a massive magmatic rock. Experiments show that after only modest axial strains (10–30%) the load-bearing framework of the strong phase disintegrates rapidly (Figs. 10a & b) as the weak phase flattens and interconnects to form micro-shear zones within the plane of shear (Le Hazif 1978, Jordan 1987). Rocks with low to moderate $\phi_w$ values that contain minerals with very high strength contrasts ($\tau_c > 10$–$100$) behave like porous sintered aggregates (Tharp 1983) except that the pores or pockets of weak phase have finite strength. The LBF–IWL boundary in Fig. 10(b) is extended steeply downward to reflect this expectation (see discussion in Handy 1990). After further strain, the LBF field shrinks upwards and to the left in Fig. 10(c) as progressively smaller volume proportions of unstable weak pockets coalesce to form interconnected layers. The time and strain to coalescence are inferred to be greater for lower values of $\tau_c$ and/or $\phi_w$ (see Ashby *et al.* 1979). The contours of normalized rock strength in the LBF field remain stationary with strain, reflecting the constant strain rate condition within the aggregate. In the IWL field, however, these contours migrate downward as progressive foliation development decreases stress concentration in the weak interconnected matrix (Jordan 1987, Handy 1990). The strain-dependent transition from a LBF to an IWL microstructure can be likened to a spontaneous, irreversible change in the internal configuration of the rock. The steady-state LBF–IWL boundary in Fig. 10(d) may therefore reflect a thermodynamic state at which the rates of strain energy dissipation and configurational entropy dissipation in the two microstructures are equal and invariant with time and strain.

The phenomenologically derived flow laws in this paper are conceptually more realistic in their treatment of microstructure than previous approaches reviewed in the Introduction. However, there are numerous points where the model of polyphase creep in this paper could be refined. The strain rate concentration function, $x$, is certainly more complicated than proposed in equation (10). There may exist additional constraints to those above that better define this function or that incorporate the nonlinear effects of stress concentration. In the absence of such constraints, $x$ may be treated as a purely empirical function of $\tau_c$ and fitted to experimental strength vs composition relations as more data become available. Another shortcoming of the model is that it is only valid for mechanical and microstructural steady state. The model does not incorporate any of the interactive feedback effects that strain-dependent changes in microstructure may have on rheology (e.g. Mitra 1978). The shape of the phases is not specified, although Tullis *et al.* (1991) point out that this may not be a serious deficiency in the case of the LBF microstructure. Deformation mechanisms other than dislocation creep are not included in the model, even though cataclasis, diffusion creep and/or pressure solution mechanisms are frequently inferred to operate in at least one phase of many mylonitic rocks (e.g. White *et al.* 1980). Fueten & Robin (1992) suggest that viscous creep by pressure solution results in a parabolic variation of composite strength with two-phase composition (their fig. 1). Stress and strain configurations deviating from the plane-strain, simple shear geometry assumed here can significantly influence the rheology of heterogeneous materials, particularly if there are fewer than the five independent, interconnected zones of weakness required to maintain strain compatibility in three dimensions (Von Mises criterion). Averaging the strain rate in all constituent phases (equation 4) simplifies the mathematics, but leads to a slight, consistent underestimation of compo-

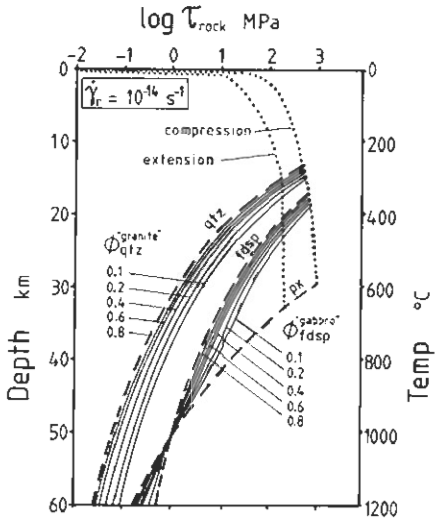


Fig. 11. Log shear strain (MPa) vs depth (km) diagrams for a crustal section comprising 'granitic' quartz–feldspar upper crustal rocks and 'gabbroic' feldspar–pyroxene lower crustal rocks. The diagram is constructed for an average geothermal gradient of 20°C $km^{-1}$ and a regional strain rate of $10^{-14}$ $s^{-1}$. Creep parameters of the hydrous end-member phases: quartzite (Jaoul *et al.* 1984), albitic feldspar (Shelton & Tullis 1981), clinopyroxene (Boland & Tullis 1986). Frictional sliding constants taken from Byerlee (1978).

site viscous strength. Finally, the concept of viscous strain energy partitioning (equation 2) and the strain energy minimization criterion for structural stability require testing in the laboratory. Synkinematic microscopy of rock-analogue materials (Means 1981) is a promising way of testing these ideas. Pending further refinement, the model of polyphase flow proposed in this paper remains a first-order approach that provides relatively simple analytical solutions to the rheology of polyphase rocks.

## APPLICATIONS TO CRUSTAL RHEOLOGY

The two-phase flow laws proposed above can be used to estimate the effect of varied rock composition on the rheology of the continental crust. In addition, the close relationship between microstructure and mineral strength contrast can be used to predict the steady-state microstructure of mylonites at various depths and compositions.

The shear stress vs depth profiles in Fig. 11 are constructed with equation (11) for the viscous creep of two-phase rocks and with the Navier–Coulomb law for frictional sliding in compression and extension (see Meissner & Strehlau 1982 for details of construction). The diagram is valid for an average geothermal gradient of 20°C $km^{-1}$ and a regional shear strain rate of $10^{-14}$ $s^{-1}$. The crustal section comprises quartz–feldspar and feldspar–pyroxene rocks, representing intermediate and basic rocks of the upper and lower continental crust, respectively. The foliation in all rocks is assumed to lie horizontally. Figure 11 includes curves for the pure constituent minerals in the rocks (dashed lines) and for selected values of $\phi_w$ from 0.1 to 0.8 (solid lines). According to the strain energy criterion of microstructural stability outlined in the sections above, only the IWL microstructure is stable over this compositional range in these rocks, so stress–depth curves for the LBF microstructure are not shown.

The curves in Fig. 11 indicate that rock composition, in addition to geothermal gradient and regional strain rate affect the viscous strength of the crust and the depth of the transition from frictional sliding to viscous creep. In quartz–feldspar rocks, as little as 10–20 vol.% of quartz reduces the composite viscous strength to less than half of that of feldspar and significantly raises the depth of the frictional to viscous transition from that of a pure feldspar rock (Fig. 11). The viscous strength contrast between quartz and feldspar is sufficiently high ($8 < \tau_c < 40$) to justify the simple assumption that quartz governs the bulk strength for all two-phase compositions with $\phi_w$ greater than 0.1. Clast–matrix microstructures are expected to predominate in quartz–feldspar rocks, except where syntectonic metamorphic reactions induce growth of weaker phases at the expense of feldspar (e.g. fig. 5 in Handy 1990). In gabbroic rock, the disparate activation energies of plagioclase and pyroxene cause mineral strength contrasts to vary from 35 at 600°C (20 km depth) to unity at 900°C (50 km depth) for the regional shear strain rate of $10^{-14}$ $s^{-1}$. At these depths and temperatures, pyroxene is expected to form boudins and clasts in weak matrix of interconnected feldspar. For temperatures greater than 900°C at the equiviscous point, the relative strength of pyroxene and feldspar inverts, and pyroxene is predicted to be the weaker interconnected phase.

The predictive quality of Fig. 11 is limited by the simplifying assumptions underlying equation (11) and the poor accuracy of the extrapolated flow laws for the constituent phases (Paterson 1987). Nevertheless, the predictions are confirmed by observations in naturally deformed rocks: quartz and feldspar are inferred to be the weakest, interconnected phases, respectively, in granitic and gabbroic tectonites deformed under conditions ranging from the upper-greenschist to granulite facies (e.g. fig. 9b in Handy & Zingg 1991).

There are many potential applications of the theory in this paper to other geological problems, ranging from the behaviour of kinematic indicators in mylonite to the interpretation of microstructural gradients across mylonitic shear zones. The phenomenological approach developed here may provide a realistic conceptual basis for future experimental and theoretical studies of microstructural stability in mylonite.

*Acknowledgements*—Many people shared their time generously in discussing with me various aspects of polyphase flow. In particular, D. Olgaard, M. S. Paterson and S. M. Schmid took the trouble to mull over some of the problems encountered in earlier versions of this manuscript. The comments of the journal reviewers, G. Mitra and Anonymous, clarified the text and aided my efforts to render the geometric assumptions consistent with the mathematical derivations. To all of the aforementioned, a hearty thank you, especially to those theoretical purists who remained beneficent in the face of my phenomenological excursions! This research was supported by a Profil-2 grant (Project No. 21-30598.91) from the Swiss National Science Foundation.

## REFERENCES


Ashby, M. F., Gandhi, C. & Taplin, D. M. R. 1979. Fracture mechanism maps and their construction for F.C.C. metals and alloys. *Acta metall.* **27**, 699–729.

Bilby, B. A., Eshelby, J. D. & Kundu, A. K. 1975. The change of shape of a viscous ellipsoidal region embedded in a slowly deforming matrix having different viscosity. *Tectonophysics* **28**, 265–274.

Boland, J. N. & Tullis, T. E. 1986. Deformation behaviour of wet and dry clinopyroxene in the brittle to ductile transition region. In: *Mineral and Rock Deformation: Laboratory Studies (The Paterson Volume)* (edited by Hobbs, B. E. & Heard, H. C.). *Am. Geophys. Un. Geophys. Monogr.* **36**, 35–50.

Byerlee, J. 1978. Friction of rocks. *Pure & Appl. Geophys.* **116**, 615–626.

Carter, N. L. & Tsenn, M. C. 1987. Flow properties of continental lithosphere. *Tectonophysics* **136**, 27–63.

Christie, J. M., Ord, A. & Koch, P. S. 1980. Relationship between recrystallized grainsize and flow stress in experimentally deformed quartzite. *Trans. Am. Geophys. Un.* **61**, 377.

Cobbold, P. R. 1983. Kinematics and mechanical discontinuity at a coherent interface. *J. Struct. Geol.* **5**, 341–349.

Einstein, A. 1909. Eine neue Bestimmung der Moleküldimensionen. *Ann. Physik* **19**, 289–306.

Einstein, A. 1911. Berichtigung zu meiner Arbeit: "Eine neue Bestimmung der Moleküldimensionen". *Ann. Physik* **34**, 591–592.

Exner, H. E. 1972. Analysis of grain- and particle-size distributions in metallic materials. *Int. Metall. Rev.* **17**, 25–42.

Freeman, B. 1987. The behaviour of deformable ellipsoidal particles in three-dimensional slow flows: Implications for geological strain analysis. *Tectonophysics* **132**, 297–309.

Fueten, F. & Robin, P. Y.-F. 1992. Finite element modelling of a pressure solution cleavage seam. *J. Struct. Geol.* **14**, 953–962.

Gay, N. C. 1968. Pure shear and simple shear deformation of inhomogeneous viscous fluids. 1. Theory. *Tectonophysics* **5**, 211–234.

Griffith, T. J., Davies, R. & Basset, M. B. 1979. Analytical study of effects of pore geometry on tensile strength of porous materials. *Powder Metall.* **22**, 119–123.

Handy, M. R. 1987. The structure, age and kinematics of the Pogallo Fault Zone, Southern Alps, northwestern Italy. *Eclog. geol. Helv.* **80**, 593–632.

Handy, M. R. 1990. The solid-state flow of polymineralic rocks. *J. geophys. Res.* **95**, 8647–8661.

Handy, M. R. 1992. Correction and addition to "The solid-state flow of polymineralic rocks". *J. geophys. Res.* **97**, 1897–1899.

Handy, M. R. & Zingg, A. 1991. The tectonic and rheological evolution of an attentuated cross section of the continental crust: Ivrea crustal section, southern Alps, northwestern Italy and southern Switzerland. *Bull. geol. Soc. Am.* **103**, 236–253.

Hill, R. 1965. Continuum micro-mechanics of elasto-plastic polycrystals. *J. Mech. Phys. Solids* **13**, 89–101.

Hirth, G. & Tullis, J. 1992. Dislocation creep regimes in quartz aggregates. *J. Struct. Geol.* **14**, 145–160.

Hobbs, B. E. & Ord, A. 1988. Plastic instabilities: implications for the origin of intermediate and deep focus earthquakes. *J. geophys. Res.* **93**, 10,521–10,540.

Hutchinson, J. W. 1976. Bounds and self-consistent estimates for creep of polycrystalline materials. *Proc. R. Soc. Lond.* **A348**, 101–127.

Jaoul, O., Tullis, J. & Kronenberg, A. 1984. The effect of varying water content on the behaviour of Heavitree quartzite. *J. geophys. Res.* **89**, 4298–4312.

Jordan, P. G. 1987. The deformational behaviour of bimineralic limestone–halite aggregates. *Tectonophysics* **135**, 185–197.

Jordan, P. G. 1988. The rheology of polymineralic rocks—an approach. *Geol. Rdsch.* **77**, 285–294.

Kröner, E. 1961. Zur plastischen Verformung des Vielkristalls. *Acta metall.* **9**, 155–161.

Le Hazif, R. 1978. Deformation plastique de system biphase Fe–Ag. *Acta metall.* **36**, 247–257.

Means, W. D. 1981. The concept of steady-state foliation. *Tectonophysics* **78**, 179–199.

Means, W. D. & Dong, H. G. 1982. Some unexpected effects of recrystallization on the microstructures of materials deformed at high temperature. *Mitt. geol. Inst. ETH Univ. Zürich* **239a**, 206–208.

Meissner, R. & Strehlau, J. 1982. Limits of stresses in continental crusts and their relation to the depth–frequency distribution of shallow earthquakes. *Tectonics* **1**, 73–89.

Mercier, J.-C. C., Anderson, D. A. & Carter, N. L. 1977. Stress in the lithosphere: inferences from the steady-state flow of rocks. *Pure & Appl. Geophys.* **115**, 199–226.

Mitra, G. 1978. Ductile deformation zones and mylonites: The mechanical processes involved in the deformation of crystalline basement rocks. *Am J. Sci.* **278**, 1057–1084.

Molinari, A., Canova, G. R. & Ahzi, S. 1987. A self-consistent approach of the large deformation polycrystal viscoplasticity. *Acta metall.* **35**, 2983–2994.

Nye, J. F. 1953. The flow law of ice from measurements in glacier tunnels, laboratory experiments and the Jungfrau borehole experiment. *Proc. R. Soc. Lond.* **219**, 477–489.

Ord, A. & Christie, J. M. 1984. Flow stresses from microstructures in mylonic quartzites of the Moine Thrust zone, Assynt area, Scotland. *J. Struct. Geol.* **6**, 639–654.

Paterson, M. S. 1987. Problems in the extrapolation of laboratory rheological data. *Tectonophysics* **133**, 33–43.

Price, R. H. 1982. Effects of anhydrite and pressure on the mechanical behaviour of synthetic Rocksalt. *Geophys. Res. Lett.* **9**, 1029–1032.

Prior, D. J., Knipe, R. J. & Handy, M. R. 1990. Estimates of the rates of microstructural change in mylonites. In: *Deformation Mechanisms, Rheology and Tectonics* (edited by Knipe, R. J. & Rutter, E. H.). *Spec. Publs geol. Soc. Lond.* **54**, 309–319.

Ramsay, J. G. & Huber, M. I.. 1987. *The Techniques of Modern Structural Geology, Volume 1: Strain Analysis.* Academic Press, London.

Rutter, E. H. & Brodie, K. 1987. The role of transiently fine-grained reaction products in syntectonic metamorphism: natural and experimental examples. *Can. J. Earth Sci.* **24**, 556–564.

Schmid, S. M., Panozzo, R. & Bauer, S. 1987. Simple shear experiments on calcite rocks: rheology and microfabric. *J. Struct. Geol.* **9**, 747–778.

Shelton, G. & Tullis, J. 1981. Experimental flow laws for crustal rocks. *Trans. Am. Geophys. Un.* **62**, 396.

Stocker, R. L. & Ashby, M. F. 1973. On the rheology of the upper mantle. *Rev. Geophys. & Space Phys.* **11**, 391–426.

Strömgård, K. 1973. Stress distribution during formation of boudinage and pressure shadows. *Tectonophysics* **16**, 215–248.

Tharp, T. M. 1983. Analogies between high temperature deformation of polyphase rocks and the mechanical behaviour of porous powder metal. *Tectonophysics* **96**, T1–T11.

Treagus, S. H. & Sokoutis, D. 1992. Laboratory modelling of strain variation across rheological boundaries. *J. Struct. Geol.* **14**, 405–424.

Tullis, T. E., Horowitz, F. G. & Tullis, J. 1991. Flow laws of polyphase aggregates from end member flow laws. *J. geophys. Res.* **96**, 8081–8096.

Twiss, R. D. 1977. Theory and applicability of a recrystallized grain-size paleopiezometer. *Pure & Appl. Geophys.* **115**, 227–244.

Twiss, R. J. 1986. Variable sensitivity piezometric equations for dislocation density and subgrain diameter and their relevance to olivine and quartz. In: *Mineral and Rock Deformation: Laboratory Studies (The Paterson Volume)* (edited by Hobbs, B. E. & Heard, H. C.). *Am. Geophys. Un. Geophys. Monogr.* **36**, 247–261.

Urai, J. L., Means, W. D. & Lister, G. S. 1986. Dynamic recrystallization of minerals. In: *Mineral and Rock Deformation: Laboratory Studies (The Paterson Volume)* (edited by Hobbs, B. E. & Heard, H. C.). *Am. Geophys. Un. Geophys. Monogr.* **36**, 161–200.

Weertman, J. 1968. Dislocation climb theory of steady-state creep. *Trans. Am. Soc. Metals* **61**, 681–694.

Weijermars, R. 1991. The role of stress in ductile deformation. *J. Struct. Geol.* **13**, 1061–1078.

Weijermans, R. 1992. Progressive deformation in anisotropic rocks. *J. Struct. Geol.* **14**, 723–742.

Wenk, H.-R., Canova, G., Molinari, A. & Kocks, U. F. 1989. Viscoplastic modelling of texture development in quartzite. *J. geophys. Res.* **94**, 17,895–17,906.

Wenk, H.-R., Bennett, K., Canova, G. R. & Molinari, A. 1991. Modelling plastic deformation of peridotite with the self-consistent theory. *J. geophys. Res.* **96**, 8337–8349.

White, S. 1976. The effects of strain on the microstructures, fabrics and deformation mechanisms in quarzites. *Phil. Trans. R. Soc.* **A283**, 69–86.

White, S. 1979. Difficulties associated with paleo-stress estimates. *Bull. Mineral.* **102**, 210–215.

White, S. H., Burrows, S. E., Carreras, J., Shaw, N. D. & Humphreys, F. J. 1980. On mylonites in ductile shear zones. *J. Struct. Geol.* **1**, 175–187.